

Star Formation and the ISM in Four Dwarf Irregular Galaxies

L. M. Young

Physics Department, New Mexico Institute of Mining and Technology, Socorro, NM 87801

lyoung@physics.nmt.edu

L. van Zee

Astronomy Department, Indiana University, Bloomington, IN 47405

vanzee@astro.indiana.edu

K. Y. Lo

*Institute of Astronomy and Astrophysics, Academia Sinica, Taipei, Taiwan ROC; and
National Radio Astronomy Observatory, Charlottesville, VA 22903*

flo@nrao.edu

R. C. Dohm-Palmer

Astronomy Department, University of Minnesota, Minneapolis, MN 55455

rdpalmer@astro.umn.edu

Michelle E. Beierle

Physics Department, New Mexico Institute of Mining and Technology, Socorro, NM 87801

mbeierle@nmt.edu

ABSTRACT

We present new, high sensitivity VLA observations of HI in four dwarf galaxies (UGCA 292, GR8, DDO 210, and DDO 216) and we use these data to study interactions between star formation and the interstellar medium. HI velocity dispersions and line shapes in UGCA 292, GR8, and DDO 210 show evidence that these three galaxies contain both warm and cool or cold HI phases. The presence of the cold neutral medium is indicated by a low-dispersion ($3\text{--}6\text{ km s}^{-1}$) HI component or by the Gauss-Hermite shape parameter $h_4 > 0$. Contrary to expectations, we find no trend between the incidence of the low-dispersion

(colder) phase and the star formation rate in five dwarf galaxies. The colder HI phase may be a necessary ingredient for star formation, but it is clearly not sufficient. However, there is a global trend between the star formation rate of a galaxy and the incidence of asymmetric HI profiles. This trend probably reflects kinetic energy input from young massive stars. Numerical simulations show that the effects of rotational broadening (finite angular resolution) are minimal for these galaxies. Simulations are also used to estimate the errors in the column densities of the high-dispersion and the low-dispersion HI phases.

Subject headings: galaxies: individual (UGCA 292, GR 8, DDO 210, DDO 216)
— galaxies: kinematics and dynamics — galaxies: dwarf

1. Introduction

Among the dwarf galaxies we find an impressive variety of optical morphologies, colors, gas contents, star formation rates and gas depletion timescales. Youngblood & Hunter (1999) found a variation of more than three orders of magnitude in the star formation rate per unit area of nearby dwarf irregulars. The star formation rates of individual galaxies have varied by factors of more than 10, both increasing and decreasing, over a Hubble time (Mateo 1998). The Local Group contains some galaxies with evidence for recent star formation but no sign of neutral gas, such as the Fornax dwarf spheroidal (Stetson, Hesser, & Smecker-Hane 1998; Young 1999). It also contains some relatively gas-rich galaxies with little to no known star formation activity, such as DDO 210 and DDO 216 (van Zee 2000). What happens in the interstellar medium (ISM) to cause such wide variations in the gas consumption timescales? The interplay between gas properties and star formation is one of the more interesting unsolved issues in the evolution of dwarf galaxies. We investigate this issue by careful study of the properties of the ISM in a sample of four dwarf irregular galaxies and comparison with their current star formation activity.

Star formation activity in dwarf galaxies is expected to take place in molecular gas, just as it does in our own Galaxy. However, molecular gas is normally not directly detectable in the lowest mass (lowest metallicity) dwarf galaxies (Taylor, Kobulnicky, & Skillman 1998; Vidal-Madjar et al. 2000). On the other hand, studies of our own Galaxy show that one can learn a great deal about the ISM from HI. Clark (1965) and Radhakrishnan, Murray, Lockhart, & Whittle (1972) found that Galactic HI emission profiles often have a high-dispersion (10 km s^{-1}) optically thin HI component superposed on a low-dispersion (3 km s^{-1}) optically thick component. The low-dispersion component also appears in absorption against a continuum source, whereas the high-dispersion component does not commonly appear in

absorption. The spatial distribution of the low-dispersion component is highly clumped; it does not appear along every line of sight, but the high dispersion component is ubiquitous.

Emission and absorption spectra can be used to estimate the spin temperatures of these components. The low dispersion component arises in a cold neutral medium (CNM) of temperature ~ 100 K, and the high dispersion component arises in a warm neutral medium (WNM) of temperature few thousand K (Kulkarni & Heiles 1988). A recent review of observational and theoretical evidence is given by Wolfire, McKee, Hollenbach, & Tielens (2002). There is some evidence that a portion of the WNM may be in a thermally unstable temperature range $500 \lesssim T_{kin} \lesssim 5000$ K, rather than the thermally stable temperature range $5000 \lesssim T_{kin} \lesssim 8000$ K (Heiles & Troland 2002; Kritsuk & Norman 2002; Gazol, Vázquez-Semadeni, Sánchez-Salcedo, & Scalo 2001). However, there seems to be no disagreement that Galactic HI encompasses a variety of temperatures.

The key connection between this HI work and what we hope to learn about star formation in the dwarf galaxies is that *the cold phase of HI is usually assumed to be a necessary ingredient for star formation* (Wolfire, McKee, Hollenbach, & Tielens 2002; Parravano 1988, 1989; Dickey, Mebold, Stanimirovic, & Staveley-Smith 2000; Elmegreen 2002a). The reason is that molecular gas must form out of the cold HI rather than the warm (Glover 2002). Indeed, Elmegreen (2002b) asserts that star formation must inevitably occur if a cold phase is present. In our own Galaxy there is evidence that the CNM is intimately associated with molecular gas, as the abundance of the CNM peaks in the molecular ring (Dickey et al. 2002). Thus, the amount and distribution of the CNM in dwarf galaxies may reveal something about their star formation potential.

The CNM/WNM phase structure has been studied in many extragalactic systems via the traditional emission/absorption techniques (Dickey & Brinks 1993; Braun & Walterbos 1992; Mebold et al. 1997; Dickey, Mebold, Stanimirovic, & Staveley-Smith 2000). The two phases can also be detected in HI emission spectra by virtue of the fact that they have different velocity dispersions; even when they occur at nearly the same radial velocity, the superposition produces a distinct non-Gaussian line shape with a narrow peak and broad wings. In this way the cold and warm HI phases have been detected in a number of nearby spirals (Braun 1997) and 500 pc below the plane of our own Galaxy (Lockman 2002). Braun (1997) shows the spatial distribution of the HI associated with the CNM in nearby spirals. Many high velocity clouds also show evidence for CNM and WNM; clumpy HI with linewidths $\lesssim 5$ km s⁻¹ is superposed on more smoothly distributed HI with larger linewidths (Wakker & Schwarz 1991; de Heij, Braun, & Burton 2002; Braun & Burton 2000).

Detailed studies of HI line profiles in the nearby dwarf galaxies Leo A and Sag DIG (Young & Lo 1996, 1997) (YL96, YL97) show features remarkably similar to Galactic HI

profiles. A broad HI component with a dispersion $\sigma \sim 8\text{--}10 \text{ km s}^{-1}$ is ubiquitous in these galaxies. A narrower HI component of $\sigma \sim 3\text{--}5 \text{ km s}^{-1}$ is concentrated into cloud-like structures of size 200–300 pc, located usually (but not always) near regions of star formation activity in Leo A and Sag DIG. Thus, the velocity dispersions and the spatial distributions of the two HI components are exactly analogous to the properties of Galactic WNM and CNM. Sternberg, McKee, & Wolfire (2002) have constructed theoretical models of the ISM in Leo A and Sag DIG, assuming that the gas must be in hydrostatic equilibrium in the galaxies’ gravitational potentials and assuming heating and cooling rates appropriate for their metallicities. These theoretical models predict the coexistence of cold and warm HI phases in the dwarfs, in agreement with our observations. Sternberg et al. have also made novel use of the HI properties of Leo A and Sag DIG to constrain the shape of the dwarfs’ dark matter halos.

The evidence described above suggests that the ISM in nearby dwarf galaxies does indeed contain CNM and WNM phases of HI in accordance with theoretical models. Furthermore, the two phases can be distinguished in HI emission spectra. The CNM is not the raw material for star formation itself but it is commonly assumed to be the raw material from which molecular gas is made. Therefore, we hypothesize that dwarf galaxies which contain greater amounts of CNM should have higher star formation rates, in the same way and for the same reasons that the molecular gas contents of spiral galaxies are positively correlated with their $H\alpha$ or far-IR luminosities (Kennicutt 1998). The primary focus of this paper is to test that hypothesis.

We investigate the properties of the HI gas in four nearby dwarf irregular galaxies through careful study of their HI line profiles. This paper presents the highest quality HI images (best sensitivity and spectral resolution) of DDO 216 (Pegasus dIrr), DDO 210, UGCA 292 (CVn dwarf A), and GR8 (DDO 155). The HI line shapes in three of these dwarfs are parametrized by fitting the profiles with two Gaussian components of different dispersions and also with Gauss-Hermite polynomials. We study the effects of ISM properties on star formation, and the effects of star formation on ISM properties, by comparing the HI line shapes to star formation activity on local (spatially resolved) and global (galaxy vs. galaxy) scales. We also present numerical simulations which quantify the reliability of the double-Gaussian decomposition and the effects of rotational broadening.

2. Sample Selection

Using the line profiles to reveal the properties of the interstellar medium requires, among other things, high signal-to-noise spectra (Appendix A) which are negligibly distorted by

beam smearing effects. Beam smearing distorts the shape of the line profile when there is a large velocity gradient within one angular resolution element (Takamiya & Sofue 2002; Gentile et al. 2002). Thus, we selected nearby HI-bright galaxies with projected rotation velocities comparable to or smaller than 20 km s^{-1} , the intrinsic width of the HI line in dwarf galaxies (Lo, Sargent, & Young 1993; Hoffman et al. 1996; van Zee et al. 1997a).

In order to gain perspective on the relationship between star formation and the ISM, and to test the hypothesis that more of the CNM would be found in galaxies with higher star formation rates, we also selected galaxies to span a range of $\text{H}\alpha$ luminosities. The resulting sample includes two galaxies of high star formation rate (GR8, UGCA 292) and two galaxies of low star formation rate (DDO 210, DDO 216). Basic properties of these galaxies are found in Table 1. DDO 216 and DDO 210 are sometimes classified as “transition” systems with optical properties intermediate between those of dwarf irregulars and dwarf spheroidals (Mateo 1998). Other members of this class include the Antlia dwarf, Phoenix, and LGS 3. UGCA 292 is the most distant member of the sample, and the only one which is not considered a member of the Local Group. Analyses of the recent star formation histories of GR8 and DDO 216 have been carried out by Dohm-Palmer et al. (1998) and Gallagher et al. (1998), respectively. Tolstoy et al. (2000) show a new, deep color-magnitude diagram of DDO 210. Dohm-Palmer et al. (2003) discuss the recent star formation history of UGCA 292.

3. Observations and Data Reduction

3.1. HI data

All four galaxies were observed with the National Radio Astronomy Observatory’s Very Large Array (VLA)¹ in its C and D configurations in 1995 and 1999. These new data offer greatly improved sensitivity over older observations (Lo, Sargent, & Young 1993; Carignan, Beaulieu, & Freeman 1990) which were made in the mid-1980s. Table 2 gives specific dates, configurations, and times on source for our new data. Each galaxy was observed in one pointing centered roughly on the optical center of the galaxy. Nearby point sources were observed every 30 to 45 minutes for use as phase calibrators. The absolute flux scale was set by observations of the sources 0137+331 or 1331+305 (whichever was closer to the galaxy in question) and bandpass calibration was determined from those same sources. All data cali-

¹The National Radio Astronomy Observatory is operated by Associated Universities, Inc., under cooperative agreement with the National Science Foundation.

bration and image formation was done using standard calibration tasks in the AIPS package. Initial imaging revealed which channel ranges were free of HI line emission. Continuum emission was subtracted directly from the raw uv-data by making first order fits to the line-free channels.

The calibrated data were Fourier transformed using several different uvdata weighting schemes chosen to enhance the spatial resolution or the sensitivity to large-scale structures. Dirty images were cleaned down to a residual level of 0.8 to 1.0 times the rms noise fluctuations. Table 3 shows the velocity range covered for each galaxy as well as the linear resolution (FWHM of the synthesized beam) and rms noise level in the final image cubes. All galaxies were observed at 1.3 km s^{-1} velocity resolution.

To determine if the total flux density was recovered in the HI synthesis observations, total integrated flux profiles were constructed from the lowest resolution HI data cubes using the GIPSY task FLUX. Figure 1 shows integrated HI spectra for all four galaxies. Their integrated HI fluxes, center velocities, and line widths are given in Table 4. In all four cases our integrated HI fluxes are greater than published single dish fluxes. Our HI flux for GR8 is within 10% of that measured by Tift & Cocke (1988), and the difference can be plausibly attributed to noise and/or calibration uncertainties. The single dish HI flux of UGCA 292 was measured by van Zee et al. (1997b) using the wrong coordinates. The velocities of DDO 210 and DDO 216 are so close to zero that confusion with Galactic HI renders single dish HI fluxes highly uncertain. Thus, there is no convincing evidence that our VLA maps have missed very extended distributions. The four sample galaxies span the full range of $M(\text{HI})/L_B$ that are known for dwarf galaxies, from the gas-rich UGCA 292 with $M(\text{HI})/L_B = 7$ to the gas-poor DDO 216 with $M(\text{HI})/L_B = 0.3$.

Moment maps of the data cubes are shown in Figures 2 through 5. The moment maps were constructed from blanked cubes, where the signal was identified based on spatial continuity between channels. In order to include even the faint, low signal-to-noise emission, each data cube was smoothed to a resolution of twice the beam prior to automatic clipping at the 2σ level. The resultant cubes were then interactively blanked to remove spurious noise spikes. A conditional transfer was applied to blank the corresponding locations in the original data cubes. Moment maps of the blanked cubes were created with the GIPSY task MOMENTS.

3.2. Optical Broadband and H α data

Optical images of the four galaxies in this sample were obtained during several observing runs at KPNO.² The images for three of the four galaxies in this sample are presented in van Zee (2000); briefly, broad band and narrow band images of DDO 210, DDO 216, and UGCA 292 were obtained with the KPNO 0.9m telescope with the T2KA CCD. The images have a spatial scale of 0.688" per pixel, and typical seeing of 1.5–2.0". The optical images of GR 8 used in this paper, kindly provided by J. J. Salzer, were also obtained with the T2KA CCD on the KPNO 0.9m and have similar depth and spatial resolution. Plate solutions for the optical images were derived from coordinates of at least 10 stars listed in the APM catalog³ and are accurate to 0.5".

As in van Zee (2001), the H α luminosities listed in Table 1 were calculated from the observed H α flux within large apertures and thus contain H α emission from both diffuse and concentrated HII regions. On average, the diffuse emission contributes approximately 50% of the total H α emission from dwarf irregular galaxies (Youngblood & Hunter 1999; van Zee 2000). Star formation rates were calculated from the H α luminosities using the conversion factor from Kennicutt (1998):

$$\text{SFR} = 7.9 \times 10^{-42} L(\text{H}\alpha) M_{\odot} \text{ yr}^{-1}. \quad (1)$$

The current star formation rates of the galaxies in this sample range from near zero (DDO 210, SFR < 0.000003 M $_{\odot}$ yr $^{-1}$ and DDO 216, SFR \sim 0.00003 M $_{\odot}$ yr $^{-1}$) to a few thousandths of a solar mass per year (UGCA 292, SFR \sim 0.0023 M $_{\odot}$ yr $^{-1}$ and GR 8, SFR \sim 0.0040 M $_{\odot}$ yr $^{-1}$). In fact, the estimated star formation rates of DDO 210 and DDO 216 are so low that statistical uncertainties in their star formation rates are substantially larger than the measurement uncertainties in the H α fluxes of Table 1. In a standard Salpeter initial mass function, only 6% of the total mass in young stars (0.1 to 100 M $_{\odot}$) occurs in stars of mass greater than 25 M $_{\odot}$. The star formation rates of DDO 210 and DDO 216 are small enough that only one or less than one HII region might be expected to be present at any time, with the corresponding problems of small number statistics. Gallagher et al. (1998) also find that the star formation rate averaged over the last 100 Myr in DDO 216 may be a factor of a few higher than the current rate derived from the H α luminosity.

²Kitt Peak National Observatory is part of the National Optical Astronomy Observatories that are operated by the Association of Universities for Research in Astronomy, Inc. under contract to the National Science Foundation.

³<http://www.ast.cam.ac.uk/~apmcat/>

4. Results

4.1. HI distributions

Figures 2 through 5 show HI distributions, overlays on optical images, and velocity fields of the four galaxies. As illustrated by these overlays, the new data cubes are significantly deeper than the data published in Lo, Sargent, & Young (1993); in particular, the new observations of DDO 210 and DDO 216 indicate HI extents larger than those shown in Lo, Sargent, & Young (1993). The HI image of GR 8 is similar to that presented in Carignan, Beaulieu, & Freeman (1990), although the present data have higher velocity resolution and are slightly deeper.

At first glance, the HI distributions appear very similar to the neutral gas distribution in other dwarf irregular galaxies (Broeils & van Woerden 1994; Broeils & Rhee 1997; van Zee et al. 1997b; Swaters et al. 2002). In each case, the HI extends well beyond the optical image (excluding possible faint stellar halos). The HI-to-optical ratio (measured at the 10^{20} atoms cm^{-2} and 25 mag arcsec^{-2} isophotes, respectively) is 2.3 for GR 8, 2.5 for UGCA 292, 2.1 for DDO 210, and 1.6 for DDO 216. The peak column densities are also typical of dIs, reaching 1.3×10^{21} atoms cm^{-2} in GR 8 and DDO 210, 3.7×10^{21} atoms cm^{-2} in UGCA 292, and only 9.2×10^{20} atoms cm^{-2} in DDO 216 in the HI maps with approximately 200 pc spatial resolution. The central column density in UGCA 292 is similar to those found in BCDs (van Zee, Skillman, & Salzer 1998; van Zee 2001), while GR 8, DDO 210, and DDO 216 have peak column densities similar to typical dIs (van Zee et al. 1997b).

The high spatial resolution images (lower left panel of Figures 2 - 5) indicate a rough correspondence between column density peaks and sites of active star formation, including the faint HII knot in DDO 210 (see van Zee et al. (1997a) for a spectrum of this enigmatic HII region). As discussed in more detail below for the cold neutral phase, a high column density appears to be a necessary, but not sufficient, condition for star formation activity.

4.2. HI kinematics

While the gas distributions in these four galaxies appear to be typical of dIs, the gas kinematics of DDO 216 and GR 8 are somewhat unusual. All four of these galaxies are at the low mass end of the gas-rich dwarf irregular class, and thus one expects the rotational component to be comparable to the velocity dispersion. In DDO 210 and UGCA 292, a clear velocity gradient is visible in both the data cubes and in the derived velocity fields (see lower right panel of Figures 2 and 4). The inclination corrected amplitudes of these velocity

gradients are small, 0.31 km s^{-1} per arcsec and 0.10 km s^{-1} per arcsec for UGCA 292 ($i = 45^\circ$) and DDO 210 ($i = 60^\circ$), respectively, but are non-negligible. Velocity gradients are also present in the velocity fields of GR 8 and DDO 216 (Figures 3 and 5). However, the gas kinematics are not as well ordered in these two galaxies; rather than a smooth velocity gradient from one side to the other, DDO 216 and GR 8 appear to have clumps of gas with similar kinematic properties (2 distinct clumps in DDO 216 and 3 clumps in GR 8). In GR8, the three clumps can be identified in the HI column density images, and in DDO 216 they can be seen in a major axis position-velocity diagram (Figure 6) at -200 km s^{-1} and at -180 km s^{-1} . The gas kinematics appear well ordered within each clump, and there is an overall kinematic profile along the optical major axis of both of these galaxies. Nonetheless, the overall impression is of random gas motions rather than a rotating disk in DDO 216 and GR 8.

In these low mass galaxies, the kinematic motions may be complicated by expanding shells and bubbles, which obscure the global dynamics. For example, in the position-velocity diagram of Figure 6 a circular structure centered at -190 km s^{-1} and $-1.5'$ ($1.5'$ northwest of the center) may be evidence for an expanding HI bubble of radius $\sim 1'$ (200 pc) and expansion velocity 10 km s^{-1} . The dynamical age of such a structure would be $2 \times 10^7 \text{ yr}$, but it is curious that there is very little star formation activity of this vintage in the galaxy (van Zee 2000; Gallagher et al. 1998).

4.3. Line shapes and velocity dispersions

Because the line profiles in DDO 216 are double-peaked throughout much of the galaxy (Figure 6), we do not attempt a detailed analysis of the velocity dispersion or profile shapes in that galaxy. But among the other three galaxies we find the usual variety of line shapes, including some which are well described by single Gaussian components and others which are not. Example spectra are shown in Figures 7, 8, and 9. Deviations from pure Gaussian shapes take the form of broader wings and a narrower peak than a simple Gaussian, and sometimes asymmetry, just as has been found for other dwarf galaxies (YL96, YL97) as well as nearby spirals (Braun 1997).

All spectra in these galaxies were fit with a single Gaussian component. Profiles were also fit with a superposition of two Gaussians of different dispersions, as was done in YL96 and YL97. In addition, we fit the HI profiles with Gauss-Hermite polynomials, which are commonly used for parametrizing the line-of-sight velocity distributions of elliptical galaxies.

The Gauss-Hermite polynomials (up to fourth order) are

$$\phi(x) = a e^{-y^2/2} \left\{ 1 + \frac{h_3}{\sqrt{6}}(2\sqrt{2}y^3 - 3\sqrt{2}y) + \frac{h_4}{\sqrt{24}}(4y^4 - 12y^2 + 3) \right\},$$

where $y \equiv (x - b)/c$ (van der Marel & Franx 1993). These functions are essentially Gaussian terms modified by an asymmetric bit whose amplitude is indicated by h_3 and a symmetric bit whose amplitude is h_4 . In the case that $h_3 = h_4 = 0$, the function is a Gaussian of amplitude a , center b , and dispersion c . If $h_3 \neq 0$ the profile is asymmetric, and if $h_4 \neq 0$ it has either a more pointed ($h_4 > 0$) or a more flat ($h_4 < 0$) top than a Gaussian. This parametrization is a useful alternative to the double-Gaussian decomposition because the h_3 and h_4 polynomials are orthogonal, so that errors in those parameters are uncorrelated (van der Marel & Franx (1993), Appendix A). In contrast, when two superposed Gaussian components are fit simultaneously, their parameters are highly correlated. The disadvantage of the Gauss-Hermite formulation is that there is no simple physical interpretation of the magnitudes of h_3 and h_4 , whereas two superposed Gaussians can be naturally interpreted in terms of gas of different velocity dispersions and/or radial velocities. All line profile fits were made using the XGAUFIT task in GIPSY.

The procedure used to distinguish profiles which are simple Gaussians from those that are not is described in YL96 and YL97. Briefly, our null hypothesis is that a simple Gaussian function is an equally good description of the profile as two Gaussians or the Gauss-Hermite functions with terms up to h_4 . The rms of the residuals is computed for all three fits over the velocity range of the line emission (roughly the central 40 of 120 channels). We divide the rms of the residuals to a single Gaussian fit by the rms of the residuals to a double Gaussian fit or a Gauss-Hermite fit. We reject the null hypothesis at the 90% confidence level in a one-tailed f-test when the ratio of the rms's is 1.27 and at the 95% confidence level when the ratio of the rms's is 1.36, for 30 degrees of freedom.

4.3.1. Gauss-Hermite analysis

Figures 10, 11, 12, 13, 14, and 15 indicate where the Gauss-Hermite fits show significant deviations from Gaussian line profiles. In DDO 210 (Figure 15), a large fraction of the profiles have positive h_4 values indicating broader wings and a narrower peak than a simple Gaussian. Very few of the profiles in DDO 210 show asymmetries (nonzero h_3 ; Figure 14).

The three prominent HI clouds of GR8 each contain young massive stars and H α emission; the stellar content of these regions is described by Dohm-Palmer et al. (1998). The southwestern clump contains the highest concentration of massive main sequence stars and is

therefore interpreted as the youngest region of star formation activity in the galaxy. This HI clump shows asymmetric profiles with $h_4 > 0$ (Figures 10 and 11), but only in the southern half of the clump near the star formation activity. The eastern HI clump has the highest concentration of blue helium-burning stars, which are somewhat older and less massive than main sequence stars of comparable luminosity. This clump shows remarkably few departures from Gaussian profile shape. The northern HI clump has the smallest massive star content, and it is interpreted as the oldest of the three regions of recent star formation activity. Line profiles throughout this entire HI clump have high degrees of asymmetry (the highest h_3 values measured in the entire sample) and $h_4 > 0$.

In UGCA 292 (Figure 12) we also find a large incidence of asymmetric profiles, $h_3 > 0$ in the western part of the galaxy and $h_3 < 0$ in the southeast. In between those two regions of asymmetric profiles, and coincident with the most luminous HII region in the galaxy, we find profiles which are indistinguishable from pure Gaussians (Figure 7). These simple Gaussian profiles have higher dispersions, 10–11 km s⁻¹, than are found elsewhere in the galaxy (7.5–9.5 km s⁻¹). Some regions of $h_4 > 0$ are found, generally offset by one beamwidth (300 pc) from HII regions (Figure 13).

UGCA 292 is the galaxy in this sample with the largest rotational velocity, and if beam smearing were important it would be expected to cause an antisymmetric pattern similar to the observed one with $h_3 > 0$ on one side of the galaxy and $h_3 < 0$ on the other. Therefore, we conducted experiments to determine the magnitude of beam smearing effects in this galaxy. The simulations described in Appendix B indicate that values of h_3 and h_4 no larger than 0.01 would be expected from beam smearing effects alone in this galaxy, whereas the observed h_3 and h_4 are up to 0.1. Furthermore, if the h_3 pattern in this galaxy were caused by beam smearing we would expect the line between $h_3 < 0$ and $h_3 > 0$ to lie along the kinematic major axis at position angle +60° (Figure 2). Instead, that line lies 50° away at position angle +110°. Thus, we believe the measured h_3 and h_4 values (and subsequent double-Gaussian decomposition) are indicative of local conditions in the gas rather than beam smearing.

4.3.2. *Double-Gaussian decomposition*

Figures 16, 17, and 18 show the fitted dispersions in the three galaxies. For profiles which are adequately described by a single Gaussian, that best-fit dispersion is plotted; for profiles which require two components at greater than 90% confidence, the two dispersions are plotted independently. In the double-Gaussian profiles, the narrower components have dispersions typically 3–6 km s⁻¹ and the broader ones are typically 8–13 km s⁻¹. As in

the cases of Leo A and Sag DIG, we find the notable result that the profiles which require only one Gaussian component have dispersions very similar to the broader component of the double-Gaussian profiles. Thus, we again find a component of HI of dispersion ~ 10 km s⁻¹ *everywhere* throughout these galaxies. In certain locations we also find an additional HI component of dispersion 3–5 km s⁻¹. We interpret these results to mean that the HI in these galaxies contains a ubiquitous high-dispersion phase, which we identify with the WNM, and a clumpy low-dispersion phase, which we identify with the CNM.

Comparison of Figures 16, 17, and 18 suggests that both the high-dispersion and low-dispersion phases in DDO 210 have dispersions lower by 1–2 km s⁻¹ than their counterpart phases in the other two galaxies.

Figures 19, 20, and 21 show the spatial distribution of the low dispersion component (CNM) with respect to the total HI column density and H α emission. From these figures it is apparent that the set of profiles in which we find the low dispersion component is almost identical to the set of profiles with $h_4 > 0$. Specifically, the distribution of the low-dispersion component in GR8 (Figure 19) is qualitatively similar to the image of nonzero h_4 in Figure 11, Figure 21 is similar to Figure 15, and Figure 20 is similar to Figure 13. The two techniques for describing deviations from simple Gaussian shapes give very similar results on where the CNM is located.

5. Discussion

5.1. Line shapes and star formation: small scale correlations

We find some correspondence between the presence of the CNM and star formation activity. Specifically, all regions of H α emission in these three galaxies are found within about one beamwidth or less of profiles containing the low dispersion component (or having $h_4 > 0$). In the case of the eastern HI clump of GR8 and its ringlike HII region, the number of such profiles is small but nonzero. In the case of UGCA 292 we find the largest spatial offsets, 300 pc, between current star formation activity and evidence of the CNM. But it is generally true that for these galaxies and for the previously studied Leo A and Sag DIG (YL96, YL97), some evidence of CNM is always near to current star formation activity.

The reverse of the previous statement is most definitely not true, however. There is not always evidence of star formation activity near to regions containing the CNM. The most dramatic example is DDO 210, where H α imaging revealed very minimal star formation activity (Table 1; van Zee (2000)) and the color-magnitude diagram also indicates a very weakly populated upper main sequence (Tolstoy et al. 2000). But DDO 210 contains ample

amounts of the CNM, as indicated in Figures 15 and 21. Other examples include the eastern portion of GR8 near RA = 12 58 42.0 (Figures 11 and 19), the northwestern quadrant of Leo A (Figure 9 of YL96), and the western half of Sag DIG (Figure 9 of YL97).

In UGCA 292, the regions of star formation activity are all near (within about one beamwidth) of asymmetric HI profiles (Figure 12). In GR8, the regions of star formation activity are all spatially coincident with asymmetric HI profiles, with the possible exception of the eastern HI clump and its ring HII region (Figure 10). In these two galaxies we find a rather close correspondence between asymmetric profiles and star formation activity. Two regions near the outer edges of DDO 210 show asymmetric profiles in places where there is no evidence of current star formation activity (Figure 14). However, in the aggregate, the evidence for small scale correlations between asymmetric profiles ($h_3 \neq 0$) and star formation activity is at least as good as, and perhaps better than, the evidence for small scale correlations between h_4 and star formation.

We do not see strong evidence of a temporal evolution in the state of the ISM. As noted in section 4.3.1, the three regions of star formation activity in GR8 have been approximately dated by their massive stellar content (Dohm-Palmer et al. 1998), and we do not see a one-to-one relationship between the stellar content and either the presence of CNM or the presence of asymmetric profiles. As stars are born and die there most certainly will be some evolution of the state of the ISM, but detecting it may require a larger dataset or one which probes different spatial and temporal scales.

5.2. Line shapes and star formation: Global correlations

We estimate, for each galaxy, the fraction of profiles that show deviations from pure Gaussian shapes. The parameters f_{h_3} and f_{h_4} (Table 5) are the number of profiles for which a nonzero h_3 or h_4 are detected at greater than 3σ confidence, divided by the number of profiles in the galaxy with signal-to-noise ratio greater than 20. The normalization is an attempt to account for differences in the overall signal-to-noise ratio of the cubes and the numbers of pixels per independent beam. For UGCA 292 and DDO 210, virtually all of the profiles with nonzero h_3 or h_4 have signal-to-noise ratios greater than 20, and f_{h_3} and f_{h_4} are less than one. However, note that strong h_3 and h_4 signatures can be detected even when the profile has a total signal-to-noise ratio less than 20 (Table 6), so that f_{h_3} and f_{h_4} are not constrained to be less than one. This effect is responsible for the large f_{h_3} and f_{h_4} in GR8.

Our data show a notable trend between a galaxy’s H α luminosity and the fraction of the profiles which are asymmetric. For this analysis we have also included Leo A and Sag DIG,

which we fitted with Gauss-Hermite polynomials in exactly the same manner as described above. Table 5 indicates, for each galaxy, the number of spectra with signal-to-noise ratios greater than 20, the fraction of spectra with significant measurements of nonzero h_3 and h_4 , and the $H\alpha$ luminosities. The data are plotted in Figures 22 and 23, where it is clear that the galaxies with larger $H\alpha$ luminosities have a greater fraction of their profiles asymmetric. In contrast, there is little correspondence between the fraction of the profiles that show evidence for CNM ($h_4 > 0$) and the $H\alpha$ luminosity.

A galaxy-wide relation between the $H\alpha$ luminosity and the fraction of profiles that show asymmetries could naturally arise if the young massive stars are injecting kinetic energy into the ISM. A young massive star located exactly in the midplane of a homogeneous gas disk might be expected to accelerate the surrounding gas in a symmetric manner, but stars outside of the midplane of real galaxies with inhomogeneous interstellar media will be more likely to accelerate the surrounding gas more strongly in some directions than in others. The result will be an asymmetric HI velocity profile.

The fits to the spectrum in Figure 9 show that one can decompose these asymmetric profiles into components typically separated by a few km s^{-1} . We can thus obtain an order-of-magnitude estimate of the kinetic energy represented by the asymmetric profiles of GR8, for example. If something like one third of the HI in GR8 is accelerated to velocities of 5 km s^{-1} with respect to the rest of the gas in the galaxy, that would require 8×10^{50} erg of kinetic energy. This value is a small fraction of the total thermal and/or turbulent energy in the HI gas, since most of the HI in the galaxy has a velocity dispersion between 8 and 13 km s^{-1} (Figure 17). Assuming the energy input from supernovae and/or stellar winds is converted into kinetic energy of the ISM at an efficiency of 10% (Lozinskaya 1992), we require 10^{52} erg of input energy, or a few canonical supernovae, to explain the asymmetric HI profiles. Given that we know massive star formation is now occurring in GR8, the energy requirements are not unreasonable. The interpretation that the asymmetric HI profiles are the result of kinetic energy input from young massive stars is plausible in this respect.

The small number of asymmetric profiles in DDO 210 can also be easily understood, given the extremely low rate of massive star formation activity. Mac Low (1999, 2002) estimates the timescale for dissipation of turbulent kinetic energy in the ISM to be on the order of 10 Myr. Thus, we expect the signatures of kinetic energy injection ($h_3 \neq 0$) to disappear very shortly after the massive stars and their HII regions disappear. Furthermore, we speculate that one might directly infer the size scales on which turbulent kinetic energy is injected into the ISM from the size scales of contiguous regions with similar h_3 values. In the present set of galaxies, those size scales are usually comparable to or smaller than our HI beam sizes (100–300 pc, Table 3).

This interpretation that the asymmetric profiles trace energy injection from young massive stars has relied on the use of $H\alpha$ to trace the star formation rate, as usual. Section 3.2 mentions, however, that the star formation rate of DDO 210 in particular is so low that the $H\alpha$ emission may not be a particularly accurate indicator of the total star formation activity. But to the extent that the most massive stars are the primary sources of kinetic energy input into the ISM, and their lifetimes are comparable to the 10 Myr timescale for dissipation of turbulent kinetic energy as mentioned above, the $H\alpha$ emission of these galaxies is an indicator of the instantaneous energy injection rate. These considerations justify the use of $H\alpha$ luminosities in Figure 22. In an analysis of CNM as a raw material for star formation activity (Figure 23), we would indeed be more interested in the *total* star formation rate rather than just the massive star formation rate. But the qualitative result coming out of Figure 23, a lack of correlation between $H\alpha$ luminosity and CNM content, would not be noticeably affected even if DDO 210 were shifted by a factor of 10 in the horizontal direction relative to the other galaxies.

5.3. Star formation and the CNM

It has sometimes been suggested that the broad (but symmetric) wings of non-Gaussian profiles — the $h_4 > 0$ shape — are caused by star formation activity stirring the gas (Dickey, Hanson, & Helou 1990). That doesn't appear to be the case in these dwarf galaxies. For example, Young & Lo (1996, 1997) showed that the HI velocity dispersions in Leo A and Sag DIG actually *decrease* in the regions of $h_4 > 0$, rather than increase. This result is contrary to what one would expect if the broad wings were due to extra kinetic energy. Furthermore, we now have the very dramatic example of the many profiles in DDO 210 with $h_4 > 0$ even though there is little or no current star formation activity. In this respect the ISM of DDO 210 is reminiscent of the ISM in high velocity clouds (Wakker & Schwarz 1991; Braun & Burton 2000; de Heij, Braun, & Burton 2002).

Rather, the evidence we have presented above suggests that the asymmetric profiles ($h_3 \neq 0$) are the result of star formation activity, whereas the narrow Gaussian component and its corresponding signature $h_4 > 0$ are due to the presence of the CNM. (Technically speaking, the measured velocity dispersions of the narrow Gaussian component do not require it to be at temperatures ~ 100 K. A dispersion of 5 km s^{-1} would, if it were entirely thermal, correspond to a temperature of 3000 K and place the gas in the thermally unstable region of the phase diagram. We would then expect the formation of cold gas from the unstable gas, and in addition there may be nonthermal gas motions within our beam.) However, it is clear that the presence of CNM does not automatically lead to star formation. The presence

of CNM seems to be a *necessary* condition for star formation– all regions of star formation activity have some CNM close by– but the CNM is clearly not a *sufficient* condition for star formation.

Lo, Sargent, & Young (1993) discussed the HI properties of nine dwarf irregular and transition dwarf galaxies, paying particular attention to the issue of their gas contents and star formation rates. They argued that it is difficult to understand the low star formation rates (both current and averaged over a Hubble time) in the faint dwarfs which have low degrees of rotational support. The present paper takes this argument one step further. One possible reason for the low star formation rates is that only the CNM in these galaxies, not the WNM, should be considered possible raw material for star formation. In Leo A and Sag DIG (YL96, YL97) we found that only 20% or so of the HI is CNM. But for DDO 210, the mystery of the low star formation rate remains. As far as we can determine without actually detecting molecular gas, the conditions in the ISM of this galaxy seem favorable for the formation of stars. Perhaps there is a significant time delay between the formation of the CNM and the formation of the molecular gas– or whatever else is the remaining necessary ingredient for star formation.

The quantitative relationships between star formation activity and the CNM are also probably complicated by the fact that energy injection into the ISM may eventually destroy the CNM. Such negative feedback may be responsible for the fact that most of the CNM in Figures 19 through 21 tends not to be located directly on top of the HII regions. This kind of negative feedback may also contribute to a lack of correlation between the global CNM content of the galaxy and the $H\alpha$ luminosity. If the CNM is destroyed by energy injection it will probably become WNM, and indeed in this respect it is significant that the models of Sternberg, McKee, & Wolfire (2002) actually require some star formation activity in order to produce WNM in the interiors of dwarf galaxies. In other words, the interstellar pressures in the interiors of the model galaxies are high enough to drive all HI into the CNM phase in the absence of some energy injection.

5.4. Constraints on dark matter halos

The theoretical analyses of Sternberg, McKee, & Wolfire (2002) incorporate radiative transfer, thermal, and ionization balance to model hydrogen gas in hydrostatic equilibrium in the gravitational potential of a small dwarf galaxy. The model galaxy contains both stars and dark matter appropriate for the Local Group dwarfs Leo A and Sag DIG, and the gas is heated and photoionized by an external radiation field. Models with either constant density dark matter cores or highly underconcentrated NFW halos produce WNM column densities

and projected HI scale heights which agree with the observed properties of Leo A and Sag DIG.

UGCA 292, GR8, and DDO 210 are broadly similar to Leo A and Sag DIG, so that all the conclusions which Sternberg et al. have made about their dark matter halos are echoed by this new set of galaxies. For example, the constant density core model favored by Sternberg et al. has a peak WNM column density of $1.4 \times 10^{21} \text{ cm}^{-2}$; for DDO 210, GR8, and UGCA 292 we find peak WNM column densities of 1.0×10^{21} , 1.2×10^{21} , and $3.4 \times 10^{21} \text{ cm}^{-2}$ respectively. The higher column densities in UGCA 292 may simply be projection effects. The model has a $1/e$ scale height in the projected HI column density of 0.6 kpc; we find HI scale heights of 500 pc for GR8, 600 pc for UGCA 292, and 240 pc for DDO 210. (These HI scale heights are measured as the geometric mean of the major and minor axes at the $1/e$ contour in the HI column density.) Thus, our new HI observations of DDO 210, GR8, and UGCA 292 show that they also require either halos with constant density cores or underconcentrated cuspy halos. The constraints may be less strong for DDO 210 than for the others, since DDO 210 is somewhat smaller in luminous mass and its HI scale heights are only half as large. The implications of these “soft cores” for the nature of dark matter are still being discussed (e.g. D’Onghia & Burkert (2003) and others).

6. Summary

We present the highest sensitivity images of HI emission from the dwarf irregular galaxies UGCA 292 and GR8 and from the transition dwarfs DDO 210 and DDO 216. The HI of DDO 216 is clearly resolved into two partially overlapping gas clouds which are separated by about 20 km s^{-1} in velocity. Many of the HI profiles in that galaxy are double-peaked.

We have analyzed the HI line profile widths and shapes in DDO 210, GR8, and UGCA 292 by fitting with Gaussians and Gauss-Hermite polynomials. Our double-Gaussian decomposition indicates that a HI component of dispersion 9–12 km s^{-1} is present everywhere in these three galaxies, and in some locations a second component of dispersion 3–5 km s^{-1} is also present. We also map out the locations of asymmetric HI profiles, indicated by $h_3 \neq 0$ in the Gauss-Hermite fits. The two fitting techniques give consistent answers: line profiles which require two Gaussians, one broad and one narrow, are also well described by $h_4 > 0$. We interpret the presence of the narrow Gaussian component ($h_4 > 0$) as evidence for the CNM. Of the six dwarf galaxies which have been studied in this way, five show evidence for the CNM.

We have estimated the effects of rotational broadening (finite angular resolution) on the

line profiles of these galaxies. Even for the galaxy with the largest velocity gradient (UGCA 292), the rotationally-induced deviations from simple Gaussian line shapes are much smaller than the deviations which are actually observed.

If the CNM is indeed the site of molecular gas formation and a necessary ingredient for star formation, one might expect a correlation between the quantity of CNM in a galaxy and its star formation rate. We estimated the amount of CNM in a galaxy by noting the fraction of profiles with $h_4 > 0$. There is no apparent relation between that fraction and the $H\alpha$ luminosity of five dwarfs spanning more than three orders of magnitude in $L_{H\alpha}$. The most striking cases are DDO 210, where we find a large incidence of CNM but very little star formation, and UGCA 292, where we find a relatively small incidence of CNM but a large star formation rate. The CNM may indeed be a necessary ingredient for star formation but it is clearly not sufficient by itself to ensure star formation.

There is a trend between the fraction of asymmetric profiles in a galaxy and $L_{H\alpha}$, in the sense that galaxies with greater star formation rates also have a greater fraction of asymmetric profiles. This result probably indicates that star formation activity is responsible for stirring the HI, and the kinetic energy involved in accelerating the HI to typical speeds of 5 km s^{-1} is reasonable for galaxies with these kinds of star formation rates. Small scale correlations between the locations of HII regions and the regions of asymmetric profiles are less clear: in some cases the asymmetric profiles are coincident with the HII regions, and in other cases the asymmetric profiles appear around the edges of the HII regions.

The three main star formation regions of GR8 have been approximately dated from their young stellar contents. We do not see a clear evolutionary sequence in the properties of the ISM in these three star formation regions. A detection of this kind of temporal evolution may require larger sample sizes which probe different spatial and/or temporal scales than what we are able to do in the present work.

Thanks to J. J. Salzer for providing the broadband and $H\alpha$ images of GR8. We appreciate the insightful comments from the referee. Support for proposal number 9044 was provided by NASA through a grant from the Space Telescope Science Institute, which is operated by the Association of Universities for Research in Astronomy, Incorporated, under NASA contract NAS5-26555. LMY and LvZ thank the Institute of Astronomy and Astrophysics, Academia Sinica, Taiwan, for travel support and hospitality. KYL thanks the Academia Sinica and the National Science Council, Taiwan, for research support.

A. Line shape measurements at low signal-to-noise ratios

A proper understanding of the uncertainties in the fitted spectral line parameters is crucial to the interpretation of most of the results in this paper. Therefore, we undertook a series of Monte Carlo simulations which were designed to show (1) the reliability of the spectral line shape parameters for profiles of low signal-to-noise ratio, and (2) the degree of correlation between the fitted parameters.

We first constructed data cubes consisting of identical model spectra with 1.3 km s^{-1} velocity resolution. The line profiles were prescribed by the Gauss-Hermite formula given in Section 4.3 with $c = 6.2 \text{ km s}^{-1}$, $h_3 = 0.05$, and $h_4 = 0.10$, values typical for the observed galaxies. Random, normally distributed noise was added to the simulated spectra in order to achieve a specified signal-to-noise ratio. For this work, signal-to-noise ratios are defined as the peak intensity of the line divided by the rms noise level. In this manner we constructed 16800 spectra at each of the signal-to-noise ratios specified in Table 6. The procedure was repeated for sets of profiles with the same signal-to-noise ratios, c , and h_4 but with $h_3 = 0.002$. All profiles were fit with the Gauss-Hermite polynomials.

Table 6 gives the fitted values of h_3 , h_4 , and their standard deviations as a function of signal-to-noise ratio. For signal-to-noise ratios of 7 and higher, the fitted h_3 and h_4 are normally distributed with standard deviations equal to the formal uncertainty reported by the fitting routine. At signal-to-noise ratios less than 7, the fitted h_3 and h_4 are no longer normally distributed. Therefore we conclude that for signal-to-noise ratios ≥ 7 , the formal uncertainties in the fitted h_3 and h_4 are reliable estimates of their errors. We also find very convincing evidence that the h_3 and h_4 parameters are indeed independent of each other. Specifically, we find no correlation between the fitted h_3 and the fitted h_4 of a given profile. The fitted h_3 values are also the same, within their errors, regardless of whether or not the h_4 term is included in the fit. Finally, the fitted h_4 and the standard deviations in h_3 and h_4 were identical for the cases $h_3 = 0.05$ and $h_3 = 0.002$.

Simulations of the double-Gaussian fitting procedure were made in a similar way. We constructed data cubes of 4225 spectra each and 1.3 km s^{-1} velocity resolution; each spectrum was filled with a superposition of two Gaussian components of 4 km s^{-1} and 11 km s^{-1} dispersions. The amplitude ratio of the two components was fixed at 1.4:1 (narrow:broad). Random noise was added to the spectra to achieve total signal-to-noise ratios of 30, 20, and 11, which is the range of signal-to-noise ratios occupied by the non-Gaussian profiles in GR8. In one set of data cubes the two components have the same velocity, and in a parallel set of data cubes they have velocities offset by 5 km s^{-1} . The spectra were then fit with a superposition of two Gaussian components.

The fitted amplitudes, center velocities, and dispersions of the two Gaussian components along with their standard deviations are presented in Table 7. As for the Gauss-Hermite fits, we find that the standard deviations in the fitted parameters are equal to the formal errors quoted by our fitting routine. We conclude that the formal errors are indeed reliable measures of the uncertainties in the parameters (at least at the signal-to-noise ratios studied here). We also note that at signal-to-noise ratios of 11, a 5 km s^{-1} velocity offset between the two components is not detectable at a 3σ confidence level. However, at signal-to-noise ratios of 20 and above this velocity offset is easily measured.

Finally, we find that the fitted amplitudes of the two Gaussian components are *strongly* correlated in the sense $A_1 + A_2 = \text{constant}$. The standard deviations in the fitted amplitudes are primarily determined by this correlation. As a result, the standard deviations of the fitted amplitudes *do not* decrease as the signal-to-noise ratio increases; rather, they are fixed at about 1.4 times the rms noise level. The situation is mildly improved for asymmetric profiles, in which cases the standard deviations in the fitted amplitudes are in the range 1.0 to 1.2 times the rms noise. The last column of Table 7 shows that the standard deviations in the column densities of the two Gaussian components range from 10% to about 40%. We would expect uncertainties in the column densities to be larger in cases where the amplitude ratio is more extreme.

B. Rotational broadening

When an object with a velocity gradient is observed at finite angular resolution, its spectral line profiles appear artificially broadened. The line profiles can also be asymmetric, which is responsible for the fact that different rotation curves for galaxies are obtained from the peak of the spectra, the median, and the mean velocity (Takamiya & Sofue 2002; Gentile et al. 2002). Therefore, we conducted simple numerical experiments to determine whether the values of h_3 and h_4 which we observe in the HI of dwarf galaxies could be artifacts of their velocity gradients.

In our present sample the largest velocity gradient is in UGCA 292, where we find $0.2 \text{ km s}^{-1} \text{ asec}^{-1}$ or 2.9 km s^{-1} per beam in the high resolution cube and 3.5 km s^{-1} per beam in the low resolution cube. The GIPSY task GALMOD was used to simulate observations of galaxies with various velocity fields and gas distributions, including the following:

- velocity gradients ranging from 0.3 to $1.2 \text{ km s}^{-1} \text{ asec}^{-1}$
- velocity fields which are solid body throughout and ones which rise linearly to a radius of about $60''$ and flatten

- uniform gas distributions as well as those that drop off by about a factor of 20 between the center and the outside edge at $100''$
- intrinsic velocity dispersions between 0.1 km s^{-1} and 10 km s^{-1} . In the absence of beam smearing, all HI spectra would be simple Gaussians of this dispersion.

All model galaxies were “observed” at 1.3 km s^{-1} velocity resolution and were smoothed to $14''$ linear resolution, similar to the high resolution cube of UGCA 292.

The synthetic spectra were fit with the Gauss-Hermite polynomials, which gave the following results. Models which closely approximate the parameters for UGCA 292 ($0.3 \text{ km s}^{-1} \text{ asec}^{-1}$ velocity gradient, intrinsic velocity dispersion $\sim 10 \text{ km s}^{-1}$) showed no significant h_3 or h_4 . All of the fitted h_3 and h_4 values were less than 0.01 and most were consistent with zero, within their uncertainties. In comparison, in the real galaxies the well-measured h_3 and h_4 are between 0.05 and 0.25. Synthetic galaxies did not have artificial h_3 and h_4 values as large as the ones found in the real galaxies unless the ratio of the velocity gradient to the intrinsic velocity dispersion was more than 10 times larger than what is found in the real galaxies. We conclude that the beam smearing which is present in the real galaxies is not large enough to explain the observed departures from simple Gaussian profiles. Rather, these departures must be indicative of local conditions in the ISM.

The velocity gradients which are present in the real galaxies also make very minor contributions to the observed line widths. The fitted dispersions of the synthetic galaxies are roughly consistent with the expectation $(\Delta v_{obs})^2 \sim (\Delta v_{true})^2 + (\Delta v_{grad})^2$, where Δv_{obs} is the observed line profile width, Δv_{true} is the intrinsic line width, and Δv_{grad} is the product of the velocity gradient and the beam size (Braun 1997). In UGCA 292, the velocity gradient amounts to about 3 km s^{-1} per beam; the observed line widths (FWHM) are $\sim 12 \text{ km s}^{-1}$ for the narrow component and 23 km s^{-1} for the broad component. Thus, the beam smearing of the velocity gradient contributes at most a few percent to the observed line widths. In this paper we therefore consider that significant changes in the line shape or width from one place to another must be indicative of changing conditions in the ISM, not global effects connected with the velocity gradient.

REFERENCES

- Braun, R. 1997, ApJ, 484, 637
- Braun, R. & Burton, W. B. 2000, A&A, 354, 853
- Braun, R. & Walterbos, R. A. M. 1992, ApJ, 386, 120

- Broeils, A. H., & Rhee, M.-H. 1997, *A&A*, 324, 877
- Broeils, A. H., & van Woerden, H. 1994, *A&AS*, 107, 129
- Carignan, C., Beaulieu, S., & Freeman, K. C. 1990, *AJ*, 99, 178
- Clark, B. G. 1965, *ApJ*, 142, 1398
- Cook, K. H. 1988, *BAAS*, 20, 743
- de Heij, V., Braun, R., & Burton, W. B. 2002, *A&A*, 391, 67
- Dickey, J. M. & Brinks, E. 1993, *ApJ*, 405, 153
- Dickey, J. M., Hanson, M. M., & Helou, G. 1990, *ApJ*, 352, 522
- Dickey, J. M., McClure-Griffiths, N. M., Gaensler, B. M., & Green, A. J. 2002, *ApJ*, in press (astro-ph/0211298)
- Dickey, J. M., Mebold, U., Stanimirovic, S., & Staveley-Smith, L. 2000, *ApJ*, 536, 756
- Dohm-Palmer, R. C. et al. 1998, *AJ*, 116, 1227
- Dohm-Palmer, R. C., van Zee, L., & Young, L. 2003, in prep.
- Dolphin, A. E. et al. 2002, *AJ*, 123, 3154
- D’Onghia, E. & Burkert, A. 2003, *ApJ*, 586, 12
- Elmegreen, B. G. 2002, *ApJ*, 577, 206
- Elmegreen, B. G. 2002, in *The Third EuroConference on the Evolution of Galaxies*, eds. G. Stasinka, G. Hensler, et al. (Dordrecht: Kluwer), in press (astro-ph/0212166)
- Elmegreen, B. G. & Parravano, A. 1994, *ApJ*, 435, L121
- Gallagher, J. S., Tolstoy, E., Dohm-Palmer, R. C., Skillman, E. D., Cole, A. A., Hoessel, J. G., Saha, A., & Mateo, M. 1998, *AJ*, 115, 1869
- Gazol, A., Vázquez-Semadeni, E., Sánchez-Salcedo, F. J., & Scalo, J. 2001, *ApJ*, 557, L121
- Gentile, G., Vergani, D., Salucci, P., Kalberla, P., & Klein, U. 2002, in *ALMA Extragalactic and Cosmology Science Workshop on Dark Matter* (astro-ph/0206477)
- Glover, S. C. O. 2002, *ApJ*, in press (astro-ph/0210493)

- Heiles, C., & Troland, T. 2002, ApJ, in press (astro-ph/0207105)
- Hoffman, G. L., Salpeter, E. E., Farhat, B., Roos, T., Williams, H., & Helou, G. 1996, ApJS, 105, 269
- Kennicutt, R. C. 1998, ARA&A, 36, 189
- Kritsuk, A. G. & Norman, M. L. 2002, ApJ, 569, L127
- Kulkarni, S. R. & Heiles, C. 1988, Galactic and Extragalactic Radio Astronomy, 95
- Lee, M. G., Aparicio, A., Tikonov, N., Byun, Y., & Kim, E. 1999, AJ, 118, 853
- Lo, K. Y., Sargent, W. L. W., & Young, K. 1993, AJ, 106, 507
- Lockman, F. J. 2002, ApJ, in press (astro-ph/0210424)
- Longmore, A. J., Hawarden, T. G., Webster, B. L., Goss, W. M., & Mebold, U. 1978, MNRAS, 183, 97
- Lozinskaya, T. A. 1992, New York: American Institute of Physics, 1992,
- Mac Low, M. 1999, ApJ, 524, 169
- Mac Low, M. 2002, in press (astro-ph/0211616)
- Mateo, M. L. 1998, ARA&A, 36, 435
- Mebold, U., Duesterberg, C., Dickey, J. M., Staveley-Smith, L., & Kalberla, P. 1997, ApJ, 490, L65
- Parravano, A. 1989, ApJ, 347, 812
- Parravano, A. 1988, A&A, 205, 71
- Radhakrishnan, V., Murray, J. D., Lockhart, P., & Whittle, R. P. J. 1972, ApJS, 24, 15
- Sternberg, A., McKee, C. F., & Wolfire, M. G. 2002, ApJS, in press (astro-ph/0207040)
- Stetson, P. B., Hesser, J. E., & Smecker-Hane, T. A. 1998, PASP, 110, 533
- Strobel, N. V., Hodge, P., & Kennicutt, R. C. 1991, ApJ, 383, 148
- Swaters, R. A., van Albada, T. S., van der Hulst, J. M., & Sancisi, R. 2002, A&A, 390, 829
- Takamiya, T. & Sofue, Y. 2002, ApJ, 576, L15

- Taylor, C. L., Kobulnicky, H. A., & Skillman, E. D. 1998, *AJ*, 116, 2746
- Tift, W. G. & Cocke, W. J. 1988, *ApJS*, 67, 1
- Tolstoy, E. et al. 1998, *AJ*, 116, 1244
- Tolstoy, E. et al. 2000, *ESO Messenger*, 99, 16
- van der Marel, R. P. & Franx, M. 1993, *ApJ*, 407, 525
- van Zee, L. 2001, *AJ*, 121, 2003
- van Zee, L. 2000, *AJ*, 119, 2757
- van Zee, L., Haynes, M. P., & Salzer, J. J. 1996, *AJ*, 114, 2479
- van Zee, L., Haynes, M. P., Salzer, J. J., & Broeils, A. H. 1997b, *AJ*, 113, 1618
- van Zee, L., Salzer, J. J., & Skillman, E. D. 2001, *AJ*, 122, 121
- van Zee, L., Skillman, E. D., & Salzer, J. J. 1998, *AJ*, 116, 1186
- Vidal-Madjar, A. et al. 2000, *ApJ*, 538, L77
- Wakker, B. P. & Schwarz, U. J. 1991, *A&A*, 250, 484
- Wolfire, M. G., McKee, C. F., Hollenbach, D., & Tielens, A. G. G. M. 2002, *ApJ*, in press
(astro-ph/0207098)
- Young, L. M. 2000, *AJ*, 120, 2460
- Young, L. M. 1999, *AJ*, 117, 1758
- Young, L. M. & Lo, K. Y. 1997, *ApJ*, 490, 710 (YL97)
- Young, L. M. & Lo, K. Y. 1996, *ApJ*, 462, 203 (YL96)
- Youngblood, A. J. & Hunter, D. A. 1999, *ApJ*, 519, 55

Table 1. Sample Galaxies

Galaxy	Alt. Name	RA J2000.0	Dec	Distance Mpc	M_B	$L(H\alpha)$ $10^{36} \text{ erg s}^{-1}$	References
UGCA 292	CVn dw A	12 38 40.0	32 46 00	3.5	−11.67	295 (3)	1, 2, 3
GR 8	DDO 155	12 58 39.4	14 13 02	2.2	−12.12	500 (25)	4, 4, 5
DDO 210	Aquarius dI	20 46 57.3	−12 49 50	0.95	−10.95	0.37 (0.32)	6, 2, 3
DDO 216	Pegasus dI	23 28 34.3	14 44 50	0.76	−12.20	3.7 (0.4)	7, 2, 3

Note. — The coordinates given here are the pointing centers used for the HI observations; they roughly correspond to the optical centers of the galaxies. All coordinates given in this paper are epoch J2000.0. All $H\alpha$ luminosities are from reddening-corrected fluxes measured in large (galaxy-size) apertures, so they include diffuse $H\alpha$ emission as well as HII regions. Uncertainties in the $H\alpha$ luminosities do not include distance; the uncertainty in the $H\alpha$ flux of GR8 is not given by Youngblood & Hunter (1999) and is arbitrarily assumed to be 5%. The M_B for UGCA 292 which is given in van Zee (2001) and the $H\alpha$ luminosity of GR8 which is given in Youngblood & Hunter (1999) have been corrected to the distances assumed here. References- 1) Dohm-Palmer et al. (2003); 2) van Zee (2001); 3) van Zee (2000); 4) Dohm-Palmer et al. (1998); 5) Youngblood & Hunter (1999); 6) Lee et al. (1999); 7) Gallagher et al. (1998)

Table 2. VLA HI Observations

Galaxy	Config	Date	Time on source hr
UGCA 292	Cs	24Jan99	13.3
GR 8	Cs	25Jan99	12.8
DDO 210	DnC	20Jan95	2.1
	Cs	25Jan99	7.5
DDO 216	D	13Mar95	2.2
	Cs	24Jan99	12.7

Table 3. HI maps

Galaxy	Velocity Range km s ⁻¹	Resolution "	Resolution pc	Noise level mJy
UGCA 292	(383,231)	17.7 × 17.4	300 × 295	0.80
		14.2 × 13.9	241 × 236	0.90
GR 8	(285, 145)	18.6 × 18.1	199 × 193	0.85
		14.8 × 14.6	158 × 156	0.96
DDO 210	(-66, -209)	27.4 × 20.8	126 × 96	1.3
		20.8 × 16.0	96 × 74	1.5
		47.5 × 37.0	218 × 170	1.6
DDO 216	(-103, -256)	25.1 × 21.2	93 × 78	0.80
		17.3 × 15.9	64 × 59	0.90
		56.2 × 52.2	207 × 192	1.0

Table 4. Global HI parameters

Galaxy	V_{sys} km s ⁻¹	ΔV_{50} km s ⁻¹	ΔV_{20} km s ⁻¹	HI Flux Jy km s ⁻¹	M(HI) M _⊙	M(HI)/L _B
UGCA 292	308.8	29.4	44.9	17.60	5.09 × 10 ⁷	7.0
GR 8	213.9	27.8	43.6	9.74	1.11 × 10 ⁷	1.0
DDO 210	-140.7	21.8	35.5	15.18	3.23 × 10 ⁶	0.87
DDO 216	-183.3	24.6	40.5	29.90	4.06 × 10 ⁶	0.34

Table 5.

Galaxy	$N_{>20}$	f_{h3}	f_{h4}	$L(\text{H}\alpha)$ $10^{36} \text{ erg s}^{-1}$
UGCA 292	250 (14.5)	0.40 (0.05)	0.31 (0.04)	300 (3)
GR8	78 (4.1)	0.96 (0.16)	1.1 (0.17)	500 (25)
DDO 210	251 (7.9)	0.08 (0.02)	0.77 (0.07)	< 0.4 (0.3)
Leo A	1037 (27.7)	0.38 (0.02)	0.93 (0.04)	9.7 (0.5)
Sag DIG	647 (15.5)	0.28 (0.02)	0.75 (0.05)	8.1 ($^{+8.1}_{-4.1}$)

Note. — $N_{>20}$ is the number of profiles with signal-to-noise ratio (fitted profile maximum / rms in line-free regions) greater than 20. In parentheses is the number of beam areas corresponding to that number of pixels. The values in parentheses after f_{h3} and f_{h4} are estimates of their uncertainties assuming Poisson statistics in counting the relevant numbers of profiles. The $\text{H}\alpha$ flux of Sag DIG is taken from Strobel, Hodge, & Kennicutt (1991), assuming a distance of 1.1 Mpc (Longmore et al. 1978; Cook 1988), and multiplied by a factor of two to account for a typical contribution of diffuse $\text{H}\alpha$ emission (van Zee 2000). Consequently the uncertainty in its $\text{H}\alpha$ flux is a factor of two. The $\text{H}\alpha$ flux of Leo A is taken from Youngblood & Hunter (1999), assuming a 5% uncertainty and a distance of 0.69 Mpc (Tolstoy et al. 1998).

Table 6. Recovery of h_3 and h_4 at low S/N

Total S/N	Fitted h_3	Fitted h_4
30	0.0501 ± 0.0124	0.0999 ± 0.0124
20	0.0501 ± 0.0186	0.0998 ± 0.0186
10	0.0504 ± 0.0378	0.0997 ± 0.0384
7	0.0506 ± 0.0552	0.100 ± 0.0572
5	0.0500 ± 0.0875	0.105 ± 0.0946

Table 7. Double-Gaussian Decomposition *vs.* Line Strength

Total S/N	Input Amp	Fitted Amp	Center km s ⁻¹	Dispersion km s ⁻¹	Column Density % Error
Symmetric Profiles					
30	17.65	17.65± 1.41	0.00± 0.16	3.99± 0.28	14
	12.32	12.32± 1.41	-0.02± 0.40	11.04± 0.67	13
20	11.76	11.76± 1.41	0.00± 0.25	3.98± 0.43	21
	8.24	8.26± 1.46	0.00± 0.63	11.10± 1.00	19
11	6.47	6.59± 1.29	0.00± 0.55	3.93± 0.81	37
	4.53	4.53± 1.41	-0.05± 1.60	11.44± 2.44	32
Asymmetric Profiles					
30	17.65	17.72± 1.05	0.00± 0.18	4.00± 0.24	11
	12.35	12.35± 0.98	-0.10± 0.60	11.00± 0.44	9
20	11.76	11.87± 1.06	0.02± 0.26	3.99± 0.37	16
	8.24	8.24± 0.99	-0.14± 0.95	11.01± 0.68	13
11	6.47	6.67± 1.18	-0.10± 1.50	3.98± 0.71	32
	4.53	4.55± 1.12	-0.50± 2.30	10.96± 1.51	24

Note. — All amplitudes are given in units of the noise level in the spectra. The top row in each pair gives values for the narrow component (input $\sigma = 4$ km s⁻¹) and the bottom row gives values for the broad component (11 km s⁻¹). Asymmetric profiles had the broad component offset in velocity by 5 km s⁻¹ from the narrow component, and that offset has been subtracted from the fitted center velocities.

Fig. 1.— Integrated HI spectra derived from the low resolution data cubes for each galaxy. These galaxies were selected for this project because their global profiles have velocity widths at the 50% level less than 30 km s^{-1} .

Fig. 2.— Moment maps of UGCA 292. (Top left) HI column density (contours) from the lowest resolution data cube overlaid on an image from the Digitized Sky Survey. The contours correspond to $0.3, 0.6, 1.2, 2.4, 4.8,$ and $9.6 \times 10^{20} \text{ atoms cm}^{-2}$. (Top right) Same, but with the column density shown in the grey scale as well as the contours. (Lower left) HI column density (contours) from the highest resolution data cube overlaid on an H α image. The contours correspond to $1., 2., 4., 8., 16.,$ and $32. \times 10^{20} \text{ atoms cm}^{-2}$. (Lower right) Velocity field of the lowest resolution data cube. The contours are marked every 5 km s^{-1} .

Fig. 3.— Moment maps of GR 8. (Top left) HI column density (contours) from the lowest resolution data cube overlaid on an R-band image. The contours correspond to $0.3, 0.6, 1.2, 2.4, 4.8,$ and $9.6 \times 10^{20} \text{ atoms cm}^{-2}$. (Top right) Same, but with the column density shown in the grey scale as well as the contours. (Lower left) HI column density (contours) from the highest resolution data cube overlaid on an H α image. The contours correspond to $1., 2., 4.,$ and $8. \times 10^{20} \text{ atoms cm}^{-2}$ (note that the inner most contour corresponds to a *depression* in the HI distribution). (Lower right) Velocity field of the lowest resolution data cube. The contours are marked every 5 km s^{-1} .

Fig. 4.— Moment maps of DDO 210. (Top left) HI column density (contours) from the lowest resolution data cube overlaid on a B-band image. The contours correspond to $0.1, 0.2, 0.4, 0.8, 1.6, 3.2, 6.4,$ and $12.8 \times 10^{20} \text{ atoms cm}^{-2}$. (Top right) HI contours and grey scale for the medium resolution data cube. Contours correspond to $0.5, 1.0, 2.0, 4.0,$ and $8.0 \times 10^{20} \text{ atoms cm}^{-2}$. (Lower left) HI column density (contours) from the highest resolution data cube overlaid on an H α image. The contours correspond to $1., 2., 4., 8.,$ and $16. \times 10^{20} \text{ atoms cm}^{-2}$. (Lower right) Velocity field of the medium resolution data cube. The contours are marked every 2.5 km s^{-1} .

Fig. 5.— Moment maps of DDO 216. (Top left) HI column density (contours) from the lowest resolution data cube overlaid on a B-band image. The contours correspond to $0.1, 0.2, 0.4, 0.8, 1.6, 3.2,$ and 6.4×10^{20} atoms cm^{-2} . (Top right) HI column density contours and grey scale for the medium resolution data cube. Contours correspond to $0.5, 1.0, 2.0, 4.0,$ and 8.0×10^{20} atoms cm^{-2} . (Lower left) HI column density (contours) from the highest resolution data cube overlaid on an $\text{H}\alpha$ image. The contours correspond to $1., 2., 4.,$ and $8. \times 10^{20}$ atoms cm^{-2} . (Lower right) Velocity field of the medium resolution data cube. The contours are marked every 5 km s^{-1} .

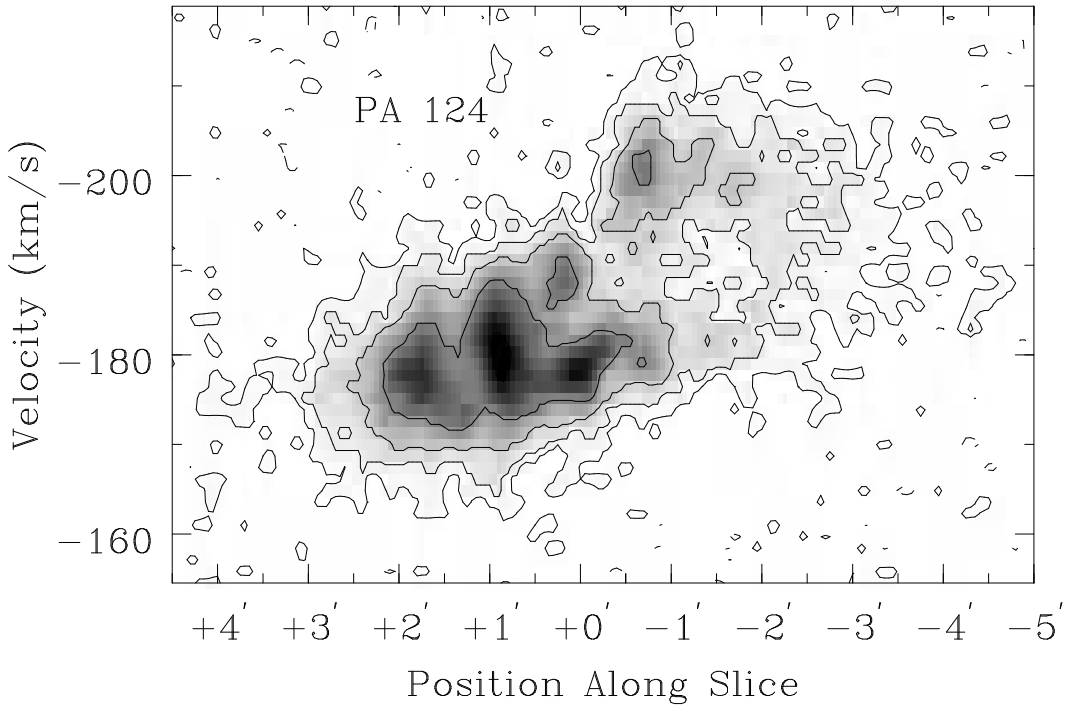


Fig. 6.— Position-Velocity diagram for DDO 216, cut at a position angle of 124° . The contours are $2\sigma, 4\sigma, 8\sigma, 16\sigma,$ and 32σ . The “bubble” to the northwest corresponds to the region where the velocity profiles are double peaked.

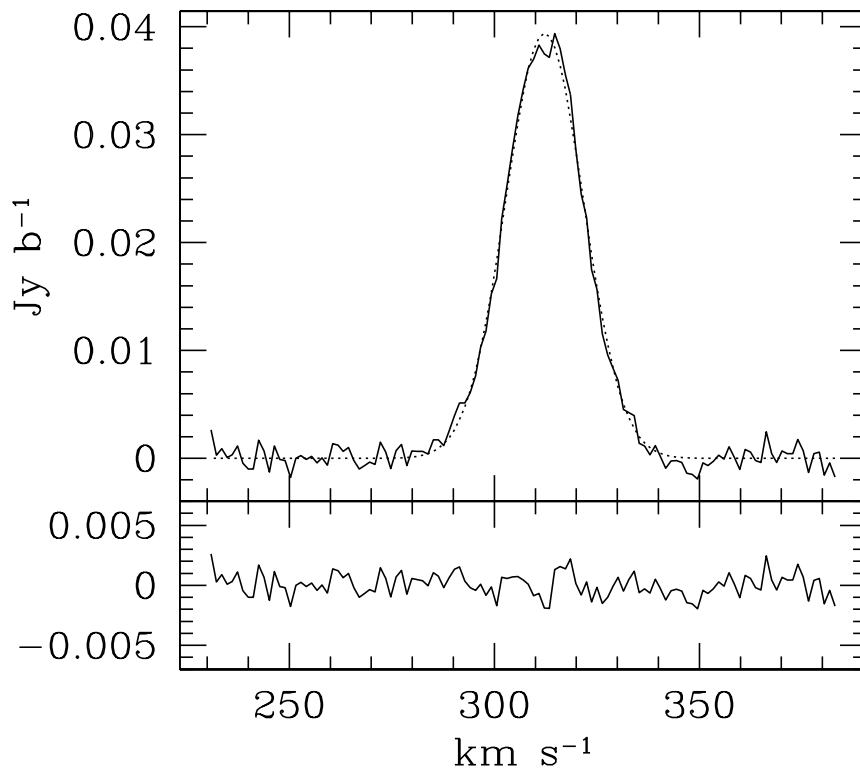


Fig. 7.— Spectrum (solid line) from UGCA 292 at RA, Dec = 12:38:40.3, +32:46:08. This spectrum is well fit by a single Gaussian component of dispersion 9.47 ± 0.09 km s⁻¹ (dotted line), and the residuals of the fit are plotted in the bottom panel. The residuals are consistent with the thermal noise level determined in the line-free channels.

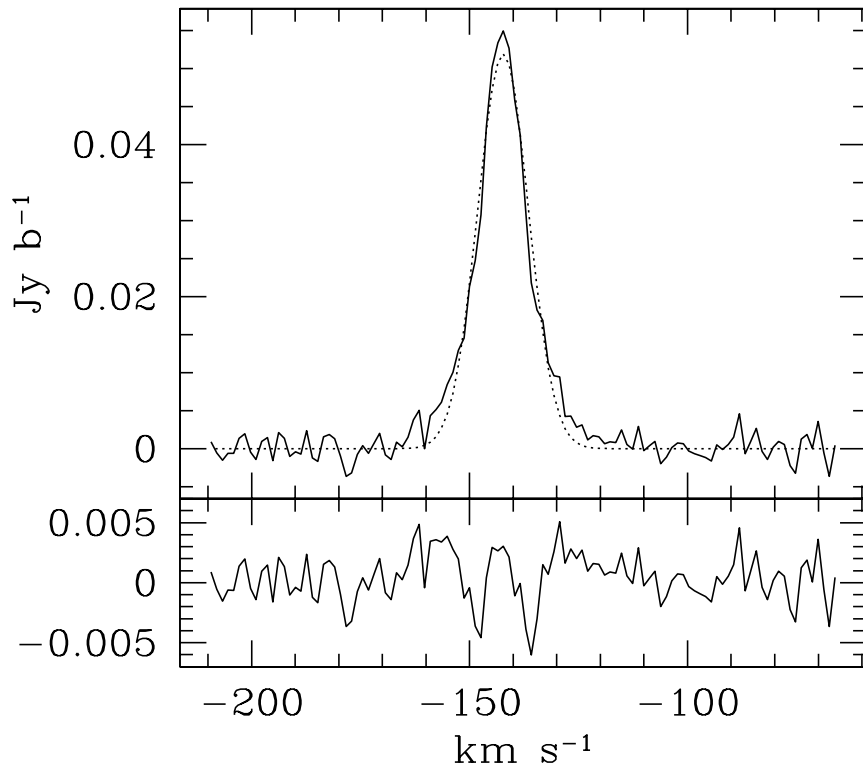


Fig. 8.— Spectrum (solid line) from DDO 210 at RA, Dec = 20:46:50.2, -12:50:57. The best fit single Gaussian model (dotted line) has a dispersion of $5.8 \pm 0.1 \text{ km s}^{-1}$, and the residuals are plotted in the lower panel. The intensity scale of the residuals is the same as for Figures 7 and 9. The f-test on the residuals indicates that, at greater than 99.9% confidence, this spectrum is better fit by a Gauss-Hermite polynomial with $h_3 = 0.00 \pm 0.01$ and $h_4 = 0.10 \pm 0.01$. The spectrum is also well fit by two Gaussian components with the same center velocities but with (amplitude, dispersion) = $(21 \pm 3 \text{ mJy b}^{-1}, 9.0 \pm 0.6 \text{ km s}^{-1})$ and $(34 \pm 3 \text{ mJy b}^{-1}, 3.8 \pm 0.3 \text{ km s}^{-1})$.

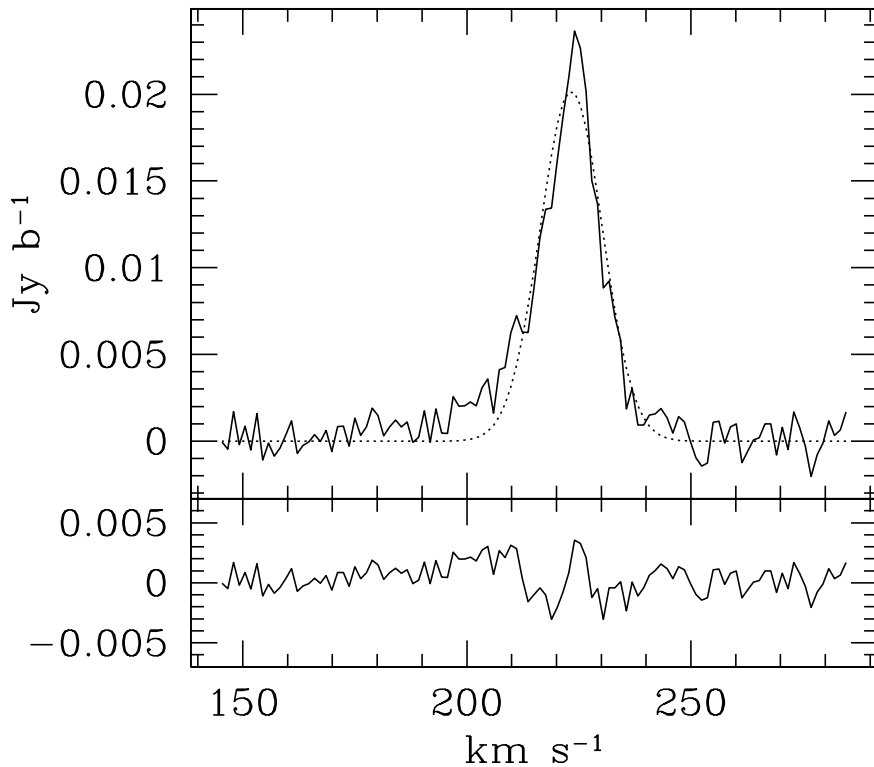


Fig. 9.— Spectrum (solid line) from GR8 at RA, Dec = 12:58:39.5, +14:13:38. The best fit single Gaussian model (dotted line) has a dispersion of $7.0 \pm 0.2 \text{ km s}^{-1}$, and the residuals are plotted in the lower panel. The f-test on the residuals indicates that, at greater than 97.5% confidence, this spectrum is better fit by a Gauss-Hermite polynomial with $h_3 = -0.10 \pm 0.02$ and $h_4 = 0.12 \pm 0.02$. The spectrum is also well fit by two Gaussian components with (amplitude, center, dispersion) = $(8 \pm 1 \text{ mJy b}^{-1}, 220 \pm 1 \text{ km s}^{-1}, 11.9 \pm 0.8 \text{ km s}^{-1})$ and $(15 \pm 1 \text{ mJy b}^{-1}, 224.3 \pm 0.2 \text{ km s}^{-1}, 4.4 \pm 0.3 \text{ km s}^{-1})$.

Fig. 10.— GR8, h_3 (boxes) on total HI column density (contours) and $H\alpha$ (greyscale). Boxes indicate the value of h_3 for profiles which, by the f-test, do require the extra terms at 90% confidence level or greater, and for which the fitted value of h_3 is greater than three times its own uncertainty. In this and subsequent box overlay figures, boxes are plotted for approximately every fourth fitted spectrum (every other one in the horizontal and vertical directions, before regridding to match the optical pixel size). Regions where no boxes are overlaid have a measurement of h_3 consistent with zero or have profiles too weak to get a good measurement of h_3 . The size of the open boxes indicates the magnitude of h_3 from -0.065 (smallest boxes) to -0.245 (largest boxes), and one filled box has $h_3 = +0.08$. The position of the spectrum in Figure 9 is indicated with a cross. The resolution of the HI data is indicated in the upper left corner.

Fig. 11.— GR8, h_4 (boxes) on HI total column density (contours) and $H\alpha$ (grayscale). As for Figure 10; the smallest boxes have $h_4 = 0.10$ and the largest boxes have $h_4 = 0.16$. Approximately one fourth of the fitted spectra are plotted.

Fig. 12.— UGCA 292, h_3 (boxes) on HI total column density (contours) and H α (grayscale, from van Zee 2000). The position of the spectrum in Figure 7 is indicated with a cross. The open boxes correspond to h_3 values from -0.039 (smallest boxes) to -0.055 (largest boxes), and the filled boxes correspond to h_3 values from 0.040 (smallest boxes) to 0.081 (largest boxes).

Fig. 13.— UGCA 292, h_4 (boxes) on HI total column density (contours) and H α (grayscale). The boxes correspond to h_4 values from 0.03 (smallest boxes) to 0.10 (largest boxes), and other items are as for Figure 12.

Fig. 14.— DDO 210, h_3 (boxes) on HI total column density (contours) and H α (greyscale). The position of the spectrum in Figure 8 is indicated with a cross. The open boxes correspond to h_3 values from -0.06 (smallest boxes) to -0.1 (largest boxes), and the filled boxes correspond to h_3 values from 0.05 (smallest boxes) to 0.12 (largest boxes).

Fig. 15.— DDO 210, h_4 (boxes) on HI total column density (contours) and H α (greyscale). The boxes correspond to h_4 values from 0.05 (smallest boxes) to 0.15 (largest boxes), and other items are as for Figure 14.

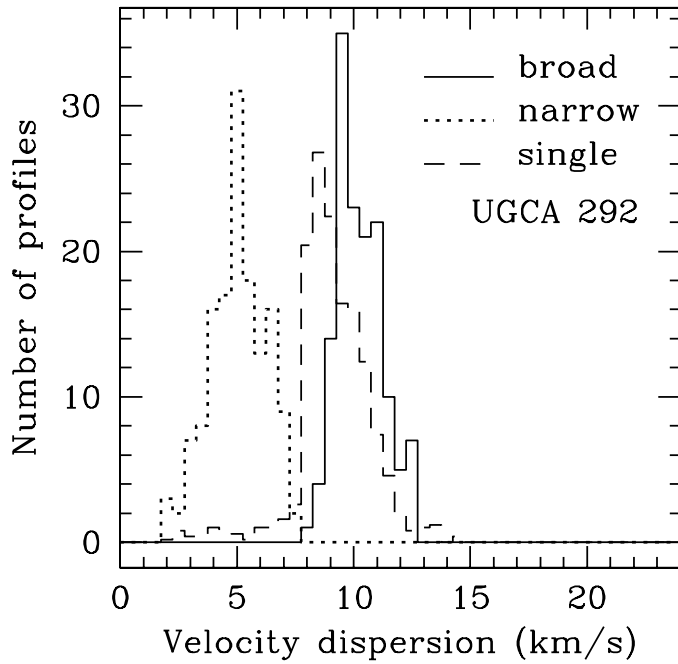


Fig. 16.— Fitted dispersions in UGCA 292. For profiles that require two components at the 90% or higher confidence level of the f-test, the dotted line shows the dispersions of the narrower component and the solid line corresponds to the dispersions of the broader component. The dashed line shows the dispersions of profiles which are adequately described by a single Gaussian component, and the vertical scale is reduced by a factor of 5.0 for this set.

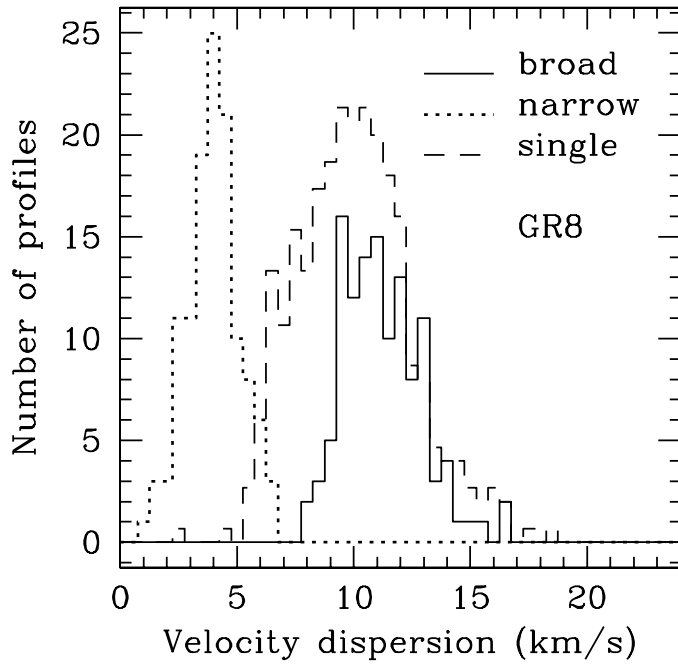


Fig. 17.— Fitted dispersions in GR8. Similar to Figure 16, but the vertical scale of the single-component profiles is reduced by a factor of 1.5.

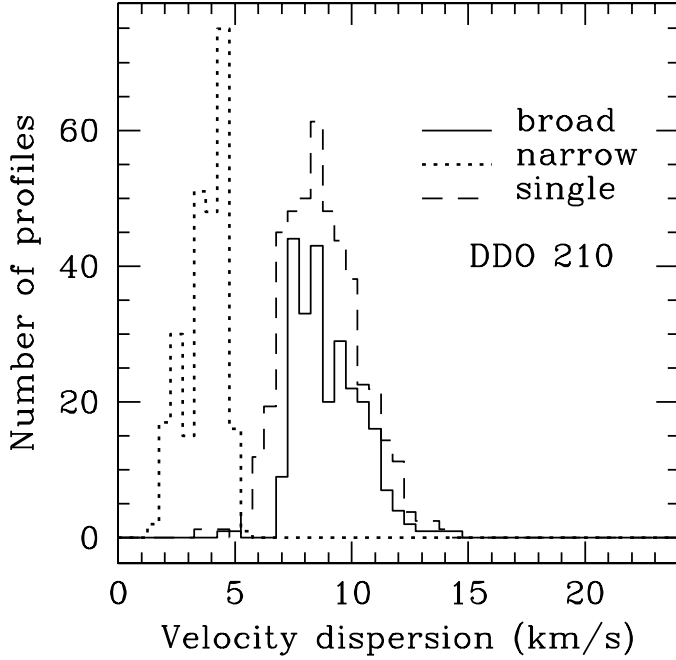


Fig. 18.— Fitted dispersions in DDO 210. Similar to Figure 16, but the vertical scale of the single-component profiles is reduced by a factor of 1.6.

Fig. 19.— GR8, column density of the narrower Gaussian component (boxes) on total HI column density (contours) and $H\alpha$. Only profiles which require the two components at greater than 90% confidence are indicated. The smallest box corresponds to a column density of approximately $5 \times 10^{19} \text{ cm}^{-2}$ and the largest to $7 \times 10^{20} \text{ cm}^{-2}$. Uncertainties in these column densities are estimated around 10–15% for the profiles with peak signal-to-noise ratios of 30, increasing to 30–40% at signal-to-noise ratio of 11 (Table 7). The position of the spectrum of Figure 9 is indicated by a cross, and the resolution of the HI data is shown in the upper left corner. As for Figures 10 through 15, 20 and 21, every fourth profile (before regriding) is plotted.

Fig. 20.— UGCA 292, column density of the narrower Gaussian component (boxes) on total HI column density (contours) and $H\alpha$. The smallest box corresponds to a column density of approximately $9 \times 10^{19} \text{ cm}^{-2}$ and the largest $1.5 \times 10^{21} \text{ cm}^{-2}$. Uncertainties in the column densities are as for Figure 19. The position of the spectrum of Figure 7 is indicated by a cross, and the resolution of the HI data is shown in the upper left corner.

Fig. 21.— DDO 210, column density of the narrower Gaussian component (boxes) on total HI column density (contours) and H α (greyscale). The smallest box corresponds to approximately $3 \times 10^{19} \text{ cm}^{-2}$ and the largest box $1.0 \times 10^{21} \text{ cm}^{-2}$. Uncertainties in these values are as for Figure 19. The position of the spectrum of Figure 8 is indicated by a cross, and the resolution of the HI data is shown in the upper left corner.

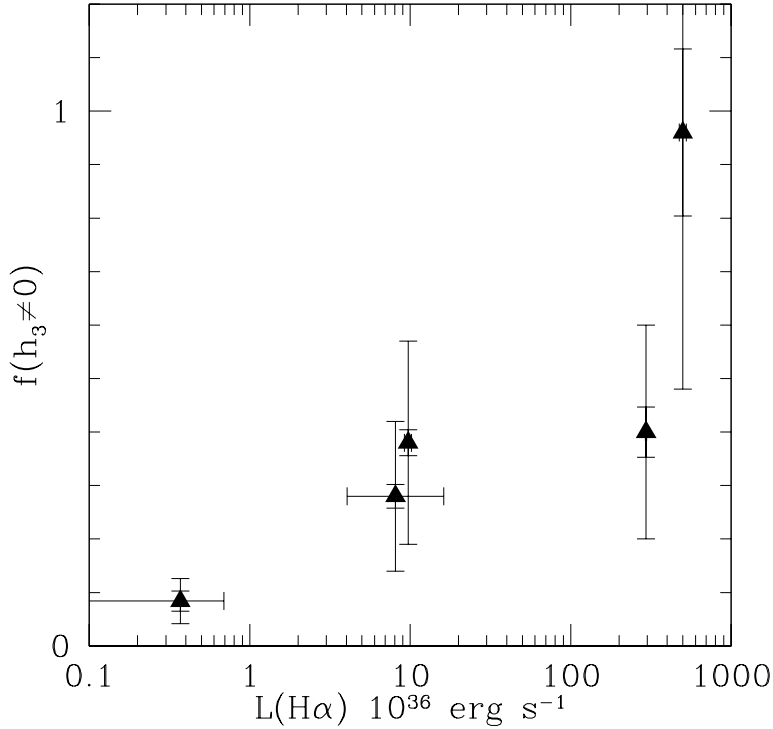


Fig. 22.— H α luminosity vs. the fraction of asymmetric profiles f_{h3} for the five galaxies in Table 5. Two error estimates are shown for f_{h3} : the smaller set of error bars corresponds to the assumption of Poisson statistics as shown in the Table. These values are likely to underestimate the true uncertainties because adjacent pixels do not contain completely independent data (though the fits are made independently). The larger set of error bars is a somewhat arbitrary assumption of a 50% error in f_{h3} .

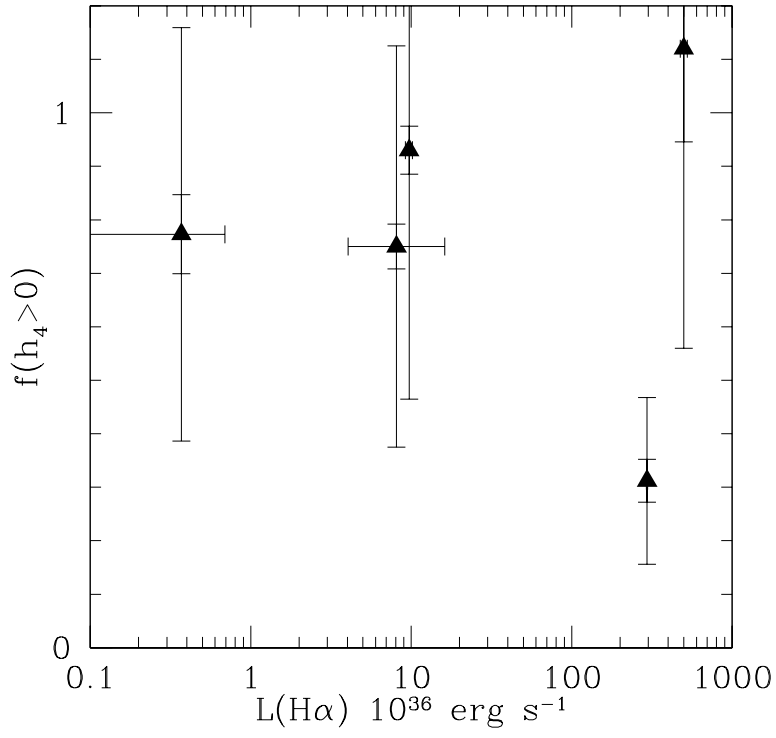


Fig. 23.— Similar to Figure 22, but for $h_4 > 0$.

This figure "f1.jpg" is available in "jpg" format from:

<http://arxiv.org/ps/astro-ph/0304266v1>

This figure "fig2.jpg" is available in "jpg" format from:

<http://arxiv.org/ps/astro-ph/0304266v1>

This figure "fig3.jpg" is available in "jpg" format from:

<http://arxiv.org/ps/astro-ph/0304266v1>

This figure "fig4.jpg" is available in "jpg" format from:

<http://arxiv.org/ps/astro-ph/0304266v1>

This figure "fig5.jpg" is available in "jpg" format from:

<http://arxiv.org/ps/astro-ph/0304266v1>

This figure "fig10.jpg" is available in "jpg" format from:

<http://arxiv.org/ps/astro-ph/0304266v1>

This figure "fig11.jpg" is available in "jpg" format from:

<http://arxiv.org/ps/astro-ph/0304266v1>

This figure "fig12.jpg" is available in "jpg" format from:

<http://arxiv.org/ps/astro-ph/0304266v1>

This figure "fig13.jpg" is available in "jpg" format from:

<http://arxiv.org/ps/astro-ph/0304266v1>

This figure "fig14.jpg" is available in "jpg" format from:

<http://arxiv.org/ps/astro-ph/0304266v1>

This figure "fig15.jpg" is available in "jpg" format from:

<http://arxiv.org/ps/astro-ph/0304266v1>

This figure "fig19.jpg" is available in "jpg" format from:

<http://arxiv.org/ps/astro-ph/0304266v1>

This figure "fig20.jpg" is available in "jpg" format from:

<http://arxiv.org/ps/astro-ph/0304266v1>

This figure "fig21.jpg" is available in "jpg" format from:

<http://arxiv.org/ps/astro-ph/0304266v1>